

The Megamaser Cosmology Project. IV. The First Direct Measurement of The Angular Diameter Distance to A Galaxy Beyond 100 Mpc

C. Y. Kuo¹, J. A. Braatz², M. J. Reid³, K.Y. Lo², J. J. Condon², C. M. V. Impellizzeri², C. Henkel⁴

¹*Department of Astronomy, University of Virginia, Charlottesville, VA 22904*

²*National Radio Astronomy Observatory, 520 Edgemont Road, Charlottesville, VA 22903, USA*

³*Harvard-Smithsonian Center for Astrophysics, 60 Garden Street, Cambridge, MA 02138, USA*

⁴*Max-Planck-Institut für Radioastronomie, Auf dem Hügel 69, 53121 Bonn, Germany*

ABSTRACT

We present the first direct measurement of the angular-diameter distance with H₂O megamaser technique to a galaxy beyond 100 Mpc in a single step without any local calibration. We image the sub-parsec scale H₂O maser disk at the center of NGC 6264 with four tracks of Very Long Baseline Interferometry (VLBI) observations. We presented an image from two of these tracks in MCP Paper III, and we add two new tracks here. With the 2.3 years of monthly Green Bank Telescope observations of the H₂O emissions in NGC 6264, we measure the centripetal accelerations of the maser lines from the accretion disk by tracking the line-of-sight velocity of each maser component as they change with time. The measured accelerations suggest that the maser disk appears to have more substructure than the masers in UGC 3789 and NGC 4258. In order to model the more complex maser disk properly and determine a precise distance and Hubble constant, we adopt a Bayesian modeling program that fits the maser disk in three dimensions. By assuming the masers follow circular orbits around the central black hole, the best fit of the data gives an angular-diameter distance of 137 ± 19 Mpc, a Hubble constant of $H_0 = 74 \pm 10$ km s⁻¹ Mpc⁻¹, and a mass of the central black hole of $(2.89 \pm 0.39) \times 10^7 M_\odot$. The result shown in this paper demonstrates the feasibility of the megamaser technique for measuring distances to galaxies deep in the Hubble flow.

Subject headings: accretion, accretion disks – galaxies: nuclei – galaxies: masers – galaxies: active – galaxies: ISM – galaxies: Seyfert

1. INTRODUCTION

Cosmology research has entered a new era since the discovery of the acceleration of the Universe (Perlmutter et al. 1999; Riess et al. 1998). “Dark Energy”, which has negative pressure and accounts for 73% of the total energy density of the Universe, is currently the best candidate to explain the cosmic acceleration, and understanding its nature has become one of the most important problems in modern astronomy and astrophysics.

There have been several very promising methods proposed to explore dark energy and its equation-of-state parameter w with high accuracy (Frieman, Turner, Huterer 2008). As pointed out by Hu (2005), among all observables for probing DE *in light of the CMB*, w is most sensitive to variations in H_0 . Hu (2005) concluded that the single most important complement to the CMB for measuring the DE equation-of-state

parameter w at $z \sim 0.5$ is a determination of the Hubble constant to better than a few percent. This insight forms the fundamental motivation for the Megamaser Cosmology project (MCP; Reid et al. 2009, Braatz et al. 2010), which aims to determine H_0 to 3% accuracy.

The key to a precise and direct determination of the Hubble constant is to measure accurate distances to galaxies well into the Hubble flow (i.e. ≥ 50 Mpc). The galaxies must be distant to reduce the contribution of the uncertainty coming from peculiar velocities. Among all the approaches to measure precise distances directly, the megamaser method pioneered by the study of NGC 4258 (Herrnstein et al. 1999) has proven to be the most effective to make precise and direct distance measurements to galaxies beyond our Local Group. In the MCP, we bypass the extragalactic distance ladder and apply the megamaser technique to galaxies in the Hubble flow, obtaining direct angular-diameter distances in a single step without any local calibration. Thus, this approach enables us to obtain an independent measurement of the Hubble constant without appealing to the Extragalactic Distance Ladder. This was not possible in the past because of insufficient sensitivity to detect H_2O megamasers at sufficiently large distances. In the past decade, the advent of the 100-m Green Bank Telescope has made this project possible.

The H_2O megamaser method involves sub-milliarcsecond resolution imaging with Very Long Baseline Interferometry (VLBI) and single-dish monitoring of H_2O maser emission from sub-parsec circumnuclear disks at the center of active galaxies. For a “simple” H_2O maser disk such as the one at the center of NGC 4258 (Herrnstein et al. 1999, Argon et al. 2007), which exhibits Keplerian rotation with the systemic masers¹ mainly lying in a single narrow ring, one can in principle determine the *geometric* distance to the galaxy by measuring four orbital parameters of the H_2O maser disk:

$$D = \frac{V_{orb}^2}{a_{sys} \Delta\theta} \sin i, \quad (1)$$

where V_{orb} is the observed orbital velocity of the systemic masers, $\Delta\theta$ and a_{sys} are the angular orbital radius and the observed acceleration of the systemic masers, respectively. In principle, V_0 , and $\Delta\theta$ can be inferred from the rotation curve of the accretion disk obtained from the VLBI imaging, i can be inferred with $\Delta\theta$ and the maser distribution in the sky (see Kuo et al. 2011), and a_{sys} can be measured with H_2O maser spectra from multi-epoch monitoring with a single-dish telescope (see Braatz et al. 2010 for details). With the megamaser technique, Herrnstein et al. (1999) has measured a distance of 7.2 Mpc to NGC 4258 with 7% uncertainty (including the systematic errors), and it is expected that, with the new VLBI data presented in Argon et al. (2007) and Humphreys et al. (2008), the uncertainty of the distance can be reduced to $\sim 3\%$ (Greenhill 2009).

In the Megamaser Cosmology Project, we aim to measure maser distances with $\sim 10\%$ or better accuracy to each of about 10 galaxies, thereby determining H_0 to $\sim 3\%$ after averaging the results. The first galaxy measured by the MCP using the megamaser technique was UGC 3789, which has a distance of 49.9 ± 7.0 Mpc (Braatz et al. 2010; Paper II hereafter). We expect to reduce the overall uncertainty to $\sim 8\%$ by including new data and better disk modeling (Reid et al. 2012). In this paper, we present the distance to NGC 6264, the first galaxy beyond 100 Mpc measured with the megamaser method. In section 2, we present our VLBI and single-dish observations. In section 3, we show the analysis of the centripetal accelerations of the masers in NGC 6264. The analyses of the Hubble constant and distance determination are presented in section 4. In section 5, we discuss the challenges of applying the maser technique to distant galaxies. Finally, we summarize the results in section 6.

¹the maser components having velocities close to the systemic velocity of the galaxy.

2. Observations and Data Reduction

2.1. VLBI Data

We observed NGC 6264 with four tracks of VLBI observations made between 2009 and 2010 using the Very Long Baseline Array (VLBA)², augmented by the 100-m Green Bank Telescope (GBT) and the Effelsberg 100-m telescope³. Two of the four tracks (BB261F and BB261H) were presented in Kuo et al. (2011), and in this paper we present the observations BB261K and BB261Q. Our final VLBI image includes the data from all four tracks. The observing parameters for the last two VLBI tracks are shown in Table 1.

The observation and data reduction procedures for BB261K and BB261Q are essentially the same as described in section 2.2 in Kuo et al. (2011). Here, we only discuss the slightly different approach to self-calibration used for the two observations presented in this paper.

Typically, in order to achieve sufficient sensitivity in the self-calibration process, we require a single maser line (linewidth $\sim 2 \text{ km s}^{-1}$) with flux density above $\sim 80 \text{ mJy}$, or a sufficient number of maser lines in a single intermediate frequency (IF) band with flux densities above $\sim 30 \text{ mJy}$. In the latter case, we achieve high enough signal-to-noise ratio (SNR) by averaging multiple maser lines in narrow ranges of both velocity and space to perform phase calibration. However, in BB261K and BB261Q, the maser lines were generally weaker than those in the previous observations on NGC 6264, and even averaging multiple maser lines in a single IF band was not sufficient to achieve sufficient SNR for self-calibration.

One way to overcome this difficulty is to utilize all maser lines with flux densities above $\sim 20 \text{ mJy}$ in *all* IF bands for self-calibration. To do this, we first remove the phase shifts due to different maser locations by dividing a model of maser positions into the data. The model division effectively moves all maser spots in consideration to the phase center of the observation, and since these masers now have the same phase, averaging the maser lines in the calibration process will increase the SNR directly.

To choose the model, the best approach would be to use as the initial guesses the maser positions obtained from phase-referencing observations of the same source, if available, or from observations at certain

²The VLBA is a facility of the National Radio Astronomy Observatory, which is operated by the Associated Universities, Inc. under a cooperative agreement with the National Science Foundation (NSF).

³The Effelsberg 100-m telescope is a facility of the Max-Planck-Institut für Radioastronomie

Table 1. Observing Parameters

Experiment Code	Date	Galaxy	Antennas ^a	Synthesized Beam (mas x mas, deg) ^b	Sensitivity (mJy) ^d	Observing Mode ^c
BB261K	2009 Nov 25	NGC 6264	VLBA, GB, EB, VLA	$1.10 \times 0.30, -9.7$	0.5	Self-cal.
BB261Q	2010 Jan 15	NGC 6264	VLBA, GB, EB	$0.80 \times 0.24, -11.8$	0.5	Self-cal.

^aVLBA: Very Long Baseline Array; GB: The Green Bank Telescope of NRAO; EB: Max-Planck-Institut für Radioastronomie 100 m antenna in Effelsberg, Germany; VLA: The Very Large Array of NRAO.

^bThe average FWHM beam size and position angle (PA; measured east of north) at the frequency of systemic masers.

^c“Self-cal.” means that the observation was conducted in the “self-calibration” mode of observation.

^dThe sensitivities were measured with a channel width of 3.6 km s^{-1} .

epochs when the self-calibration can be done easily because of stronger maser fluxes. Following this guideline, for BB261K and BB261Q, we used the averaged maser positions from BB261F and BB261H, and divided the model into the data in order to shift each maser spot to the phase center before performing self-calibration observation. Once the model subtraction and line-averaging are done, we treat the masers as a single maser spot, and follow the same calibration procedure for solving the atmospheric phase, solution editing, and imaging as described in Kuo et al. 2011. Finally, we combine the maser map obtained from BB261K and BB261Q with the one from BB261F and BB261H on the image plane by aligning the maser disks using the average position of the systemic maser features from BB261K and BB261Q with velocities between $10191.1 \text{ km s}^{-1}$ and $10198.3 \text{ km s}^{-1}$ as the reference. We present the combined data in Table 2.

2.2. GBT monitoring

We took 20 H_2O maser spectra with the GBT for NGC 6264 between 2008 November 21 and 2011 March 2. Except during the summer months when the humidity makes observations at 22 GHz inefficient, we took a spectrum on a monthly timescale. For these observations, we follow the same observing settings and data reduction procedures as in Braatz et al. (2010). Table 1 shows the observing date and sensitivity for each observation. A representative H_2O maser spectrum for NGC 6264 can be found in Figure 1 in Kuo et al. 2011.

Table 2. Sample data for NGC 6264

V_{op}^{a} (km s ⁻¹)	Θ_x^{b} (mas)	$\delta\Theta_x^{\text{b}}$ (mas)	Θ_y^{b} (mas)	$\delta\Theta_y^{\text{b}}$ (mas)	A^{c} (km s ⁻¹ yr ⁻¹)	σ_A^{c} (km s ⁻¹ yr ⁻¹)
10918.33	0.397	0.0056	-0.033	0.0141	0.00	1.00
10914.71	0.403	0.0065	0.011	0.0154	0.00	1.00
10911.09	0.407	0.0048	-0.005	0.0114	0.11	1.00
10907.47	0.399	0.0069	0.026	0.0171	0.00	1.00
10853.15	0.487	0.0037	-0.011	0.0091	0.00	1.00
10849.53	0.494	0.0036	0.003	0.0089	0.00	1.00
10845.91	0.501	0.0021	-0.027	0.0055	0.16	1.00
10842.29	0.504	0.0018	-0.023	0.0049	-0.04	1.00
10838.67	0.508	0.0042	-0.024	0.0118	-0.24	1.00
10824.19	0.537	0.0071	-0.039	0.0159	0.27	1.00
10809.70	0.550	0.0037	-0.028	0.0092	0.00	1.00
10806.08	0.561	0.0034	-0.053	0.0090	0.00	1.00
10802.46	0.572	0.0017	-0.031	0.0044	-0.09	1.00
10798.84	0.577	0.0013	-0.040	0.0034	-0.27	1.00
10793.40	0.582	0.0014	-0.028	0.0039	-0.05	1.00
10787.97	0.596	0.0046	-0.032	0.0125	0.00	1.00
10780.73	0.614	0.0031	-0.045	0.0075	-0.13	1.00
10773.49	0.632	0.0058	-0.025	0.0149	0.00	1.00
10766.25	0.654	0.0051	-0.046	0.0136	-0.26	1.00
10762.63	0.673	0.0055	-0.088	0.0142	0.00	1.00
10755.38	0.664	0.0044	-0.071	0.0117	-0.06	1.00
10751.76	0.672	0.0020	-0.052	0.0052	-0.07	1.00
10748.14	0.677	0.0035	-0.084	0.0099	0.02	1.00

Note. — Sample of data for NGC 6264. The entirety of data for all galaxies is available in the electronic version.

^aVelocity referenced to the LSR and using the optical definition (no relativistic corrections).

^bEast-west and north-south position offsets and uncertainties measured relative to the average position of the systemic masers from the BB261K and BB261Q data. Position uncertainties reflect fitted random errors only.

^cMeasured or estimated acceleration and its uncertainty for each maser component.

Table 3. GBT Observing dates and sensitivities for NGC 6264

Epoch	Date	Day Number	T_{sys} (K)	rms Noise (mJy)	Period
0	2008 November 21	0	30.9	1.7	A
1	2009 January 16	56	28.2	1.3	A
2	2009 February 3	74	35.9	1.3	A
3	2009 March 4	103	31.9	1.2	A
4	2009 March 31	130	37.8	1.4	A
5	2009 May 13	172	41.5	1.7	A
6	2009 November 7	351	44.3	1.7	B
7	2009 December 12	386	27.4	1.5	B
8	2010 January 11	416	26.3	1.1	B
9	2010 February 9	445	39.0	1.5	B
10	2010 March 7	471	28.3	1.5	B
11	2010 April 13	507	36.8	2.2	B
12	2010 May 10	534	28.2	1.2	B
13	2010 July 2	588	40.3	2.2	B
14	2010 October 30	708	40.2	1.7	C
15	2010 November 26	735	38.4	1.5	C
16	2010 December 24	763	30.3	1.5	C
17	2011 January 23	793	31.4	1.2	C
18	2011 February 7	808	42.7	1.4	C
19	2011 March 2	831	39.0	2.3	C

Note. — The rms noise values are calculated without performing Hanning smoothing to the spectra and are based on 0.33 km s^{-1} channels. We label Period A, B, and C to those times when we have continuous observations on a monthly timescale. These periods are separated by summer months during which the humidity makes observations inefficient.

3. Acceleration Analysis

3.1. Methodology

The accelerations of the H₂O maser lines measured in the megamaser technique are centripetal accelerations from circular orbits in the accretion disks. We measure these accelerations by tracking the line-of-sight velocity of each maser line as they change with time. We adopted two different methods to determine the accelerations of maser spots in this paper. The first method is what we call the *Eye-tracking* method. In this method, we first plot the velocities of maser lines as a function of time (e.g. the left panel in Fig. 1), and identify a group of data points within a particular time segment by eye that we believe to be from a particular maser line that persists over time. We then fit the trend of data points in the plot with straight lines. The slopes of the fitted lines directly give the accelerations.

The second method is the *GLOFIT* method. Here, we use a global least-square fitting program (Braatz et al. 2010; Humphreys et al. 2008) to fit multiple maser lines from multiple epochs simultaneously, and determine the accelerations of the fitted maser lines in a single step. This is the same method we used for measuring the maser accelerations in UGC 3789 (Braatz et al. 2010; Reid et al. 2012)

For NGC 6264, we adopt the GLOFIT method to measure accelerations of the systemic masers and the Eye-tracking method for the high velocity masers. We choose the GLOFIT technique for the systemic masers because accurate acceleration measurements of the systemic masers is critical for a precise Hubble constant determination with the megamaser technique, and it is the GLOFIT method that can better handle the line-blending effect of the systemic masers and determine their accelerations more accurately. On the other hand, since many high velocity maser lines are relatively isolated, and very precise acceleration measurements of these masers are not critical for accurate distance determination, to avoid the time-consuming and laborious fitting process for all high velocity maser lines, we apply the Eye-tracking method to provide good estimates of accelerations for the high velocity masers.

While it is more appropriate to adopt the GLOFIT program to measure the accelerations of the systemic masers, it may be necessary to use a different strategy to apply the method in NGC 6264 than in UGC 3789 because as a result of the joint effect of more significant blending and SNR limitations, finding stable and converging solutions is more difficult. One way to improve the situation is to fit all the maser lines in the velocity range of interest to drift with a single acceleration in the global fitting. In principle, this approach should help the program to reach convergence more efficiently and stably because the SNR of the fitting increases when we enforce a common acceleration. We have found that this is indeed the case after testing this approach with synthetic spectra generated from simulations.

Finally, the applicability of the GLOFIT program in the way described above depends critically on the assumption that masers within the selected range of spectra drift at the same rate. Therefore, to avoid systematic errors it is important to examine whether the chosen sections of spectra really satisfy this assumption. A correct verification of the constant acceleration assumption would depend on many factors including whether the masers show the same linear trend in the position-velocity (P-V) diagram (indicating they come from the same radius), the persistency of the maser spectral pattern with time, the reduced χ^2 of the fit, and the degree of line-blending. For the interested readers, we refer to Kuo 2012 (Ph.D. thesis) for details.

3.2. Acceleration Fitting for High Velocity Masers

In Figure 1, we plot the radial velocities of NGC 6264 maser peaks measured by eye as a function of time. For the blueshifted and redshifted masers, we first identify lines that are persistent in time and then fit a straight line to the data to measure the acceleration directly with the eye-tracking method. We estimate the uncertainty of the measurements by scaling the fitting error by the square root of reduced χ^2 . In Table 4, we show the measured accelerations and uncertainties.

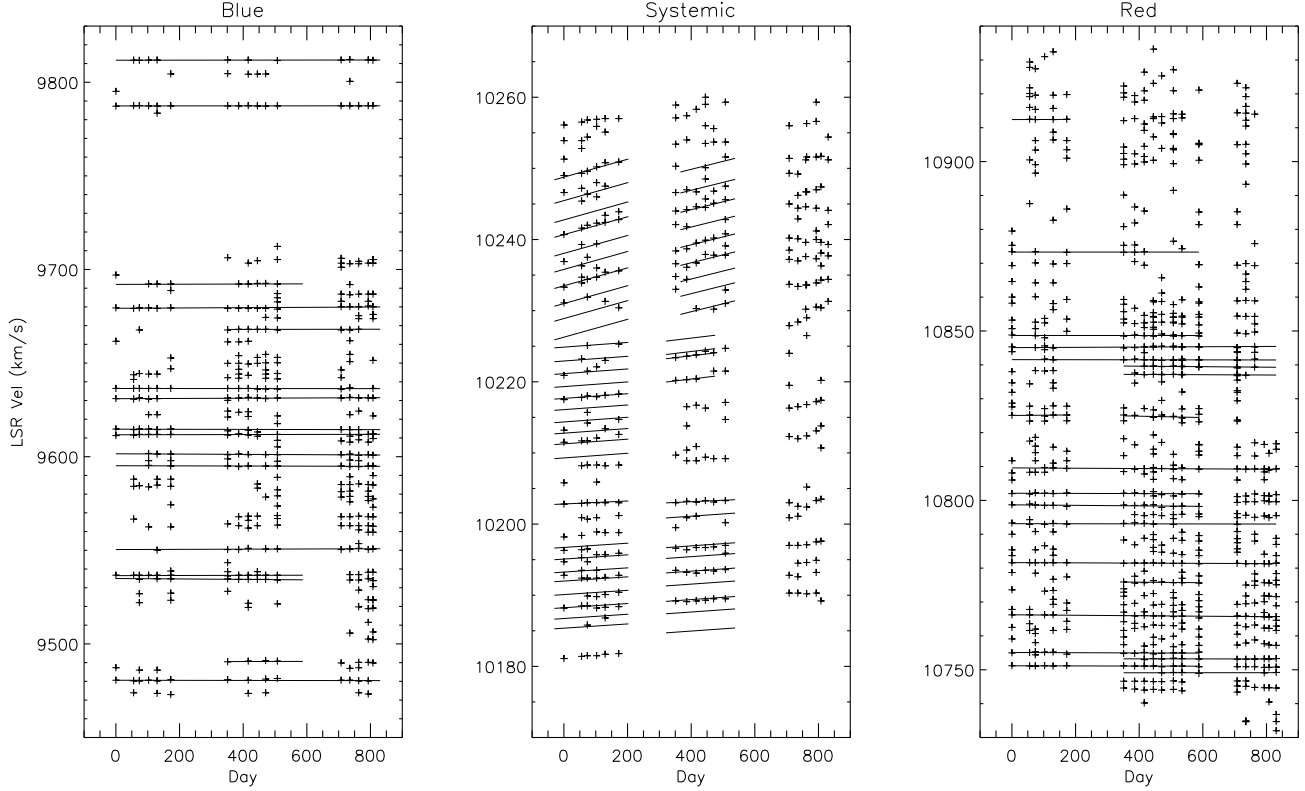


Fig. 1.— In this figure, we plot the radial velocities of NGC 6264 maser peaks as a function of time (the crosses) along with the fitting results from the eye-balling method (for the high velocity masers) or from the modified GLOFIT program (for the systemic masers). The data between Day 0 and 200 come from spectra taken in Period A; the data between Day 300 to 600 from spectra in Period B; and the data between Day 700 to 900 are from spectra in Period C.

The weighted average accelerations of the redshifted and blueshifted masers are -0.06 and $0.01 \text{ km s}^{-1} \text{ yr}^{-1}$ respectively. The rms scatter of acceleration of the redshifted and blueshifted masers are both $0.11 \text{ km s}^{-1} \text{ yr}^{-1}$. The small acceleration and rms scatter indicate that the high velocity masers are close to the mid-line of the accretion disk as expected.

When assigning the measured accelerations to the corresponding channels in the VLBI datasets, we pay attention to whether the periods over which the accelerations are measured actually bracket the epochs of

Table 4. Acceleration Measurements for the High Velocity Masers in NGC 6264

Velocity (km s ⁻¹)	Acceleration (km s ⁻¹ yr ⁻¹)	σ_{accel} (km s ⁻¹ yr ⁻¹)
9480.57	-0.09	0.07
9490.42	0.14	0.55
9536.46	0.15	0.420
9534.93	-0.44	0.17
9550.39	0.19	0.12
9595.16	-0.13	0.08
9601.54	-0.28	0.08
9611.70	0.11	0.10
9614.70	-0.12	0.06
9630.99	0.23	0.08
9636.43	-0.04	0.07
9667.88	0.09	0.10
9679.29	0.29	0.08
9692.04	0.17	0.10
9787.36	0.02	0.03
9811.77	0.05	0.06
10749.05	0.02	0.14
10751.24	-0.07	0.04
10753.28	-0.03	0.08
10755.20	-0.10	0.10
10766.50	-0.26	0.03
10776.50	-0.30	0.42
10781.77	-0.13	0.02
10793.18	-0.05	0.10
10798.96	-0.27	0.11
10802.19	-0.09	0.08
10809.58	-0.17	0.06
10824.78	0.27	0.34
10826.46	-0.75	0.73
10837.53	-0.16	0.08
10840.21	-0.27	0.06
10841.58	-0.04	0.05
10845.09	0.16	0.06
10848.68	0.00	0.11
10873.30	0.00	0.16
10912.41	0.11	0.60

Note. — The acceleration measurements for the high velocity masers. The components having velocity higher than 10745 km s⁻¹ are redshifted masers whereas those having velocity lower than 9815 km s⁻¹ are blueshifted masers

our VLBI observations. We have two tracks (BB261F & BB261H) of VLBI observations in Period A (2008 November 21 – 2009 May 13; see Table 2), two tracks (BB261K & BB261Q) in Period B (2009 November 7 – 2010 July 2) and no data in Period C (2010 October 30 – 2011 May 2). For those masers persisting over Periods A through C, we assign the measured accelerations to the corresponding VLBI channels of the data from averaging all four tracks. For those masers that persist only during Period A or B, we assign the accelerations only to the VLBI channels from observations in the respective period. For high velocity maser spots without acceleration measurements, we assume their accelerations are zero and assign them to the data from averaging all four tracks.

3.3. Acceleration Fitting for Systemic Masers

Figure 2 shows the maser spectra from Epochs 0 through 5 (Period A) and from Epochs 6 through 11 (Period B). We do not show the spectra from Period C because there is evidence that the systemic masers in this period have accelerations different from masers in Period A and B. Since we do not have VLBI data for Period C, the acceleration measurements for the systemic masers in this period are not useful for the distance determination, and thus we do not show the analysis here. Since both Periods A and B bracket two tracks of VLBI observations and the accelerations of systemic masers could change with time, we measure acceleration in Periods A and B separately. In cases where the accelerations measured in both periods within a certain velocity range are the same and the corresponding VLBI positions are consistent, we average the accelerations and VLBI positions. For those maser lines that only persist during one period, we only use the VLBI positions at this particular period for these masers in the distance and Hubble constant measurement.

To measure the accelerations, we break the spectra into distinct velocity ranges, as indicated in Figure 2, and analyze each range individually.

3.3.1. Clump 1

The results from the eye-tracking fitting suggest that the maser lines at $V \sim 10203 \text{ km s}^{-1}$ have significantly smaller acceleration ($a \sim 0.6 \text{ km s}^{-1} \text{ yr}^{-1}$) than the rest of the masers ($a \sim 1.2 \text{ km s}^{-1} \text{ yr}^{-1}$). Therefore, to fit a constant acceleration for each velocity range, we divide Clump 1 into two velocity sections: 10183.0 to 10200.2 km s^{-1} and 10200.2 to 10203.5 km s^{-1} , where $V = 10200.2 \text{ km s}^{-1}$ is at the local minimum that divides the two sub-clumps.

For the maser lines of Clump 1 within 10183.0 to 10200.2 km s^{-1} , we could not find a model to make a stable fit unless we narrow the velocity range to 10183.0 to 10197.7 km s^{-1} . This suggests that maser lines between 10197.7 and 10200.2 km s^{-1} have different accelerations than the other lines in the fitted velocity range. Since we cannot give a good constraint on the accelerations of these lines, we do not include them in the distance determination. For lines between 10183.0 and 10197.7 km s^{-1} , we fit 8 Gaussian components to the spectra and obtain an acceleration of $1.04 \pm 0.14 \text{ km s}^{-1} \text{ yr}^{-1}$. The reduced χ^2 for this fit is 1.144 (153 the degrees of freedom). For the maser lines between 10200.2 to 10203.5 km s^{-1} , we fit two Gaussian components and obtain an acceleration of $0.75 \pm 0.10 \text{ km s}^{-1} \text{ yr}^{-1}$. We overplot the acceleration measurements in this and the following subsections on top of the time-velocity plot for the systemic masers (the middle plot of Figure 1) and list the results in Table 4. We also show an example of the result of the Gaussian decomposition in the acceleration fitting with the masers in Clump 1 in Figure 3.

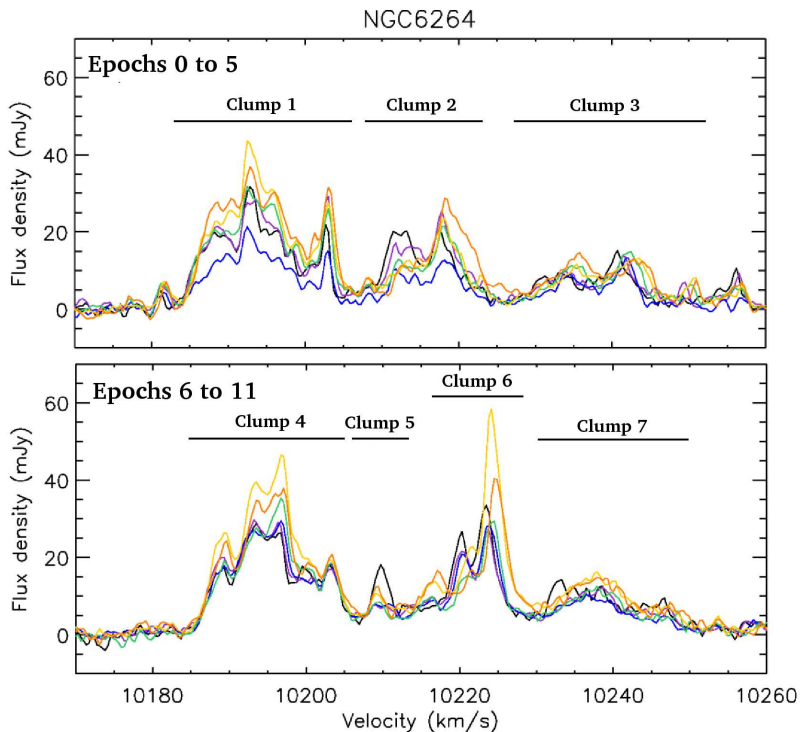


Fig. 2.— The upper panel shows the spectra from epoch 0 through 5 (purple, blue, green, yellow, and orange), and the bottom panel shows the spectra from epoch 6 through 11 (purple, blue, green, yellow, and orange). The velocity ranges of the systemic masers in Period A and B are divided into 7 clumps for the convenience of acceleration measurement.

3.3.2. Clump 2

The maser lines in Clump 2 are apparently drifting and the general pattern of the clump seems to persist with time. However, we couldn't find a good model to fit the data. The best reduced χ^2 we can achieve is 1.44, and the fitted acceleration is $1.2 \pm 0.3 \text{ km s}^{-1} \text{ yr}^{-1}$. The situation does not improve when we only fit subsets of this clump. The large reduced χ^2 suggests that our constant acceleration assumption may not hold. Therefore, for masers in this clump, we only use the VLBI channel at $V=10218.11 \text{ km s}^{-1}$ in the distance determination because it is the only line for which we have an acceleration measurement ($a=1.55 \pm 0.46 \text{ km s}^{-1} \text{ yr}^{-1}$) from the eye-tracking fitting for this clump.

3.3.3. Clump 3

Maser lines in Clump 3 have the largest acceleration among the systemic masers in NGC 6264. The acceleration is large enough that the drifting of the whole clump can be seen clearly in Figure 2. We fit ten Gaussian components with an average linewidth of 2.4 km s^{-1} to the masers between 10226.0 to $10252.3 \text{ km s}^{-1}$. The measured acceleration is $4.43 \pm 0.36 \text{ km s}^{-1} \text{ yr}^{-1}$ with a reduced χ^2 of 1.006 (314 degrees of

freedom).

3.3.4. *Clump 4*

The maser lines in Clump 4 reside within the same velocity range as Clump 1, but cover time period B, and the situation is similar. So we perform the fitting in two velocity sections: 10184 to 10201.6 km s⁻¹ and 10201.6 to 10205.5 km s⁻¹, where $V = 10201.6$ km s⁻¹ is at the local minimum that divides the two sub-clumps. For maser lines between 10184 to 10201.6 km s⁻¹, we fit 9 Gaussian components to the data and obtain an acceleration of 1.12 ± 0.18 km s⁻¹ yr⁻¹ with reduced χ^2 of 1.009.

For the masers between 10201.6 to 10205.5 km s⁻¹, we could not find a reliable fit because of severe blending. By comparing the maser spectra from Period A and Period B, we argue that since the line structure remains similar over Periods A and B at this velocity range, we are seeing the same maser lines that appear at slightly different velocities because of the acceleration. This idea is supported by the fact that the VLBI position of the masers in this velocity range from Periods A and B are very well consistent with each other. For these reasons, we assume these masers have the same acceleration ($a = 0.75 \pm 0.1$ km s⁻¹ yr⁻¹) as the masers in Clump 1 at the similar velocity range.

3.3.5. *Clump 5*

Clump 5 covers a velocity range between 10207 to 10212 km s⁻¹ and the lines within this velocity range do not show a clear sign of drifting. In addition, the line structure changes substantially over the course of time and we found it difficult to measure a reliable acceleration for this clump. We can measure significantly different accelerations, ranging from 0.4 to 4.2 km s⁻¹ yr⁻¹ by using different subsets of the spectra in the fit. This implies that we may see different lines at different epochs. Along with the fact that the VLBI positions for masers in this clump have relatively large error bars, we decide not to include these masers in the Hubble constant determination.

3.3.6. *Clump 6*

The acceleration measurement for masers in clump 6 is also not trivial, like Clump 5. We couldn't achieve a converging fit. The line structure changes substantially at epoch 10. By inspecting the spectra in Period B along with those in Period C, we discovered that the line at $V \sim 10224.1$ km s⁻¹ starts to drift at a much higher rate ($a > 7$ km s⁻¹ yr⁻¹) after epoch 9. This may be caused by newly arising lines from smaller radii of the disk. Because of this complexity, which could introduce significant systematic error in our fitting caused by maser lines with different accelerations, we do not include this group of masers in the Hubble constant determination.

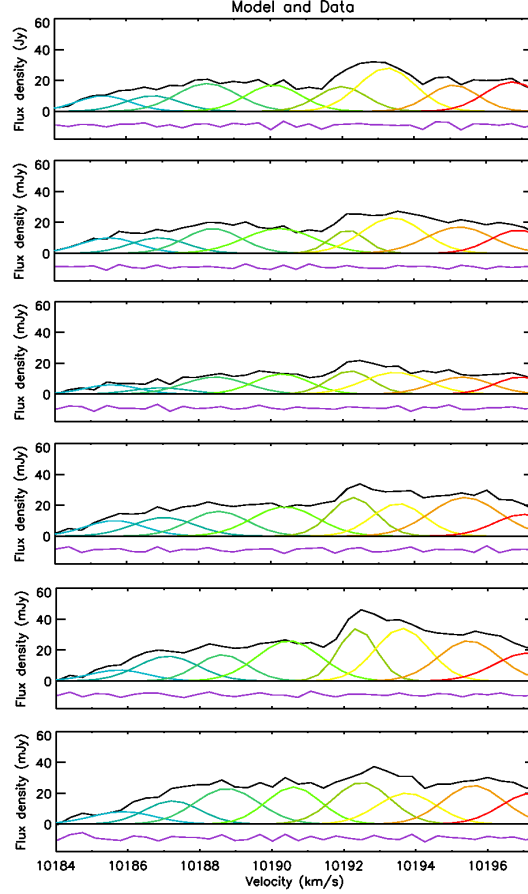


Fig. 3.— An example of the Gaussian decomposition for the acceleration measurement. In this example, we fit the masers between 10183.0 and 10197.7 km s^{−1} in the spectra. The panels from top to bottom show the spectra (black lines) from epoch 0 through 5. Each of the eight Gaussian components fitted to the data are represented by different colors. The purple curves at the bottom of each panel are the residuals from the fit.

3.3.7. Clump 7

The masers in Clump 7 cover nearly the same velocity range as Clump 3, but the drifting of the whole maser pattern becomes much less clear because of both severe blending and reduced SNR. The blending causes the line structure to become very smooth and there are only two lines that can be seen to drift clearly in the time-velocity plot (Figure 2). For this clump, we fit nine Gaussian components with an average linewidth of 2.3 km s^{−1} to the masers between 10230.5 to 10250.5 km s^{−1}. The measured acceleration is 3.96 ± 0.59 km s^{−1} yr^{−1} with a reduced χ^2 of 1.075 (180 degrees of freedom). This is consistent with the value for clump 3, and implies that masers in clumps 3 and 7 are basically the same maser emission but appear at different times.

4. Distance Determination for NGC 6264 and the Hubble Constant

4.1. The 3-Dimensional Bayesian Approach to Hubble Constant Determination

To determine the Hubble constant with the NGC 6264 data, we adopt a Bayesian approach to model the maser disk in three dimensions (Reid et al. 2012). Unlike the "ring method" used in previous result for UGC 3789 (Braatz et al. 2010), the Bayesian technique can fit a maser disk with maser clouds distributed arbitrarily across the thin disk.

The 3-dimensional nature of the modeling allows one to model the warping structure and orbital inclinations precisely if there is a sufficient number of both high velocity and systemic maser spots. Note that accurate modeling of the disk structure not only helps to measure the impact parameters (i.e. the projected separation between a maser spot and the BH) of maser spots more precisely, but also is crucial to place tight constraints on the position of the black hole and the recession velocity of the galaxy, both of which are very helpful for constraining the maser distance and Hubble constant.

The Bayesian nature of the analysis allows one to use all prior information for the model parameters to constrain the fitting more easily. In principle, the use of prior information can help guide the fitting to find the most likely solutions efficiently and reliably in the large χ^2 space which could have multiple local minimums. Furthermore, rather than seeking a single (best) solution and formal uncertainties, the Bayesian approach can directly probe the posteriori probability distribution of parameters without the assumption that the uncertainties follow a Gaussian distribution. Finally, one can model the eccentricity of the maser orbits in three dimensions, and directly measure its impact in the distance determination with the H₂O megamaser method. However, since our data is currently too noisy to allow a convergent fit for the eccentricity parameters, in this paper we will only model the maser disk with circular orbits. We will explore the effects of eccentricity in a future paper after data quality improves by including new data in the analysis.

The fitting program uses the same code for fitting the maser disk in NGC 4258 (Humphreys et al. in prep) and UGC 3789 (Reid et al. 2012). In this program, we fit the maser data including the East & North offset (x & y) of the maser positions on the sky, and the observed radial velocities (v) and accelerations (a) of the maser spots with a three dimensional model of the maser disk. We construct the model (Figure 4) by placing each maser spot at radius r and disk azimuth angle ϕ (with $\phi \approx 0^\circ$ for systemic masers and $\phi \approx 90^\circ$

Table 5. Acceleration Measurements for the Systemic Masers in NGC 6264

Clump	Velocity Range (km s ⁻¹)	Epochs	Num. of Components	Linewidth (km s ⁻¹)	Acceleration (km s ⁻¹ yr ⁻¹)	σ_{accel} (km s ⁻¹ yr ⁻¹)	χ^2_ν	d.o.f.
1	10183.0 – 10197.7	0 – 5	8	1.9	1.04	0.40	1.144	153
1	10200.2 – 10203.5	0 – 5	2	1.9	0.75	0.14	0.966	40
2	10209.1 – 10228.0	1 – 5	11	1.7	1.20	0.30	1.440	144
3	10226.0 – 10252.3	0 – 5	10	2.4	4.43	1.13	1.006	314
4	10184.0 – 10201.6	6 – 11	9	2.0	1.12	0.54	1.009	183
7	10230.5 – 10250.5	7 – 11	9	2.3	3.96	1.77	1.075	180

Note. — Col(1): The clump number; Col(2) The velocity range for acceleration measurement; Col(3) The epochs of the spectra used for fitting; Col(4) The number of Gaussian components that fit the data; Col(5) The average linewidth of fitted lines; Col(6) The best fit acceleration; Col(7) The uncertainty of the acceleration; Col(8) The reduced χ^2 of the fit; Col(9) The number of degrees of freedom of the fit.

for redshifted masers) on an elliptical orbit about a point mass (presumably a black hole) M_{BH} , with the whole system at a distance D . The center of the maser disk on the sky is (x_0, y_0) , its recession velocity is v_{sys} , and the velocity correction to the pure Hubble flow is v_{cor} .

The disk can be warped in two dimensions: the inclination warp $i(r)$ and the position-angle warp $p(r)$, each of which is specified by 3 parameters:

$$i(r) = i_0 + i_1 r + i_2 r^2, \quad (2)$$

$$p(r) = p_0 + p_1 r + p_2 r^2, \quad (3)$$

where r is the radius of the orbit in milli-arcsec. One can choose how many of these warping parameters one should actually use in the fitting depending on the degree of warping. During the fitting process, the program adjusts r and ϕ along with the above-mentioned global parameters including H_0 and M_{BH} simultaneously until the best fit is reached. Note that in choosing the set of parameters to model the maser disk, unlike what was done for modeling the maser disk in NGC 4258 in Herrnstein et al. (1999), we fit H_0 instead of using D as one of the primary parameters. Details are given in the appendix.

The program adopts a Markov chain Monte Carlo (MCMC) approach (e.g. Geyer 1992; Gilks, Richardson & Spiegelhalter 1996) to obtain the posteriori probability distribution function of the model parameters. In this approach, one fits the data in a “brute force” manner by randomly trying a large number of model parameter values. Because of the “Markov chain” nature of the parameters, the $i^{th} + 1$ trial parameter values are dependent on, and close to, the i^{th} values. In particular, this program uses the Metropolis-Hastings algorithm (e.g. Metropolis et al. 1953; Hastings 1970) to choose the Markov-chain trial parameters, and a global step-size factor in the fitting is adjusted to scale parameter steps so that an optimal Metropolis-Hastings acceptance rate of $\approx 23\%$ (Gelman, Gilks, & Roberts 1997) is achieved. This algorithm has the property that the distribution of the trial parameter values is equal to the desired posteriori probability distribution function of the parameters. In the actual fitting process, we first run 20 burn-in stages, each with 10^5 trials, in order to arrive at near optimum parameter values. After discarding the burn-in stage trials, we evaluated 10^7 MCMC trials to obtain final posteriori probability distributions. Note that the trial number is chosen to be such a large number in order to ensure we explore the parameter space sufficiently.

4.2. Hubble Constant Derived From the Bayesiann Fitting

The top panel of Figure 5 shows that the degrees of both the inclination warp and the position-angle warp appear to be relatively small from the maser map. Therefore, we fit the warp only to the linear term in Equations (3) & (4). To account for systematic uncertainties in our measurements of the positions, velocities, and accelerations of the maser spots, we estimate more realistic “error floors” of 8 mas and 16 mas for x & y , respectively, 0.8 km s^{-1} and 0.4 km s^{-1} for velocities of systemic and high-velocity maser features, and $1.0 \text{ km s}^{-1} \text{ yr}^{-1}$ for accelerations of high-velocity masers. For accelerations of systemic masers, the estimated error floors range from 0.3 to $0.7 \text{ km s}^{-1} \text{ yr}^{-1}$, depending on each individual maser clump. We add the error floors to these observational errors in quadrature before fitting the data.

We adopt *flat* priors for all parameters except for H_0 ($72 \pm 18 \text{ km s}^{-1} \text{ Mpc}^{-1}$), V_{sys} ($10196 \pm 28 \text{ km s}^{-1}$; Beers et al. 1995)⁴, and V_{cor} ($-19 \pm 300 \text{ km s}^{-1}$). The first two priors were purposely set fairly “loosely” so

⁴All velocities quote here are non-relativistic, optical definition, LSR velocities; these velocities were converted internally in the fitting program to relativistically correct values.

as not to overly constrain and dominate the fitting. The prior for V_{cor} comes from the sum of two values: a correction of -19 km s^{-1} to convert from the LSR to the cosmic microwave background frame, and an assumed value of the peculiar velocity of the galaxy expected from large scale gravitational perturbations. Since we do not have an estimate of the peculiar velocity from simulation of large scale cosmic flows, we assume the peculiar velocity to be 0 km s^{-1} with 300 km s^{-1} uncertainty.

Among the priors adopted for the Bayesian fitting, the H_0 prior especially plays an important role to get our final result. By exploring the fitting with a flat prior on H_0 and weighting the data differently, we discovered that there are two primary local minima in the χ^2 space for the H_0 parameter: one at $H_0 \sim 74 \text{ km s}^{-1} \text{ Mpc}^{-1}$ and the other at $H_0 \sim 90 \text{ km s}^{-1} \text{ Mpc}^{-1}$. Without prior information on H_0 , it is difficult to tell from the data itself which local minimum has a higher probability, and the fitting result can depend sensitively on how we weight the data, even though the weights may only change slightly. Introducing a prior on H_0 allows the fit to converge to the local minimum of $H_0 \sim 74 \text{ km s}^{-1} \text{ Mpc}^{-1}$ more stably with little influence by changes in the data weights. We expect that this situation will improve in the future when we incorporate new data for this galaxy.

Figure 5 shows the qualities of the Bayesian fitting by comparing the best fit model with the observed maser distribution, position-velocity diagram, and acceleration measurements. In general, the model matches the observations well, and the differences between the data and model are consistent with real uncertainties. The total reduced χ^2 of fit is 0.951.

The left panel in Figure 6 shows the maser distribution from overhead. As expected, the systemic masers reside at different radii because of their divergent accelerations, and the high velocity masers are located close to the mid-line of the maser disk because their accelerations are close to zero. The latter feature substantially supports the assumption made in Kuo et al. (2011) that the high velocity masers are close to the mid-line of the disk within ~ 13 degrees, and therefore the BH mass can be reliably and accurately constrained by fitting a Keplerian rotation curve to the high velocity masers. In the right panel of Figure 6, we show the warp structure with the maser spots plotted on top of the warping disk. Note that we increase the disk inclination by 5 degrees in order to show the warp structure more clearly.

We show the *posteriori* probability distribution for H_0 from the Bayesian fitting in the left panel of Figure 7. The posteriori probability distribution is slightly asymmetric about the peak of the distribution, which has a 68% confidence range of $9 \text{ km s}^{-1} \text{ Mpc}^{-1}$ centered at $H_0 = 74 \text{ km s}^{-1} \text{ Mpc}^{-1}$. The mode and the median of the posteriori probability distribution are $73 \text{ km s}^{-1} \text{ Mpc}^{-1}$ and $74 \text{ km s}^{-1} \text{ Mpc}^{-1}$, respectively.

We found that the best fit H_0 has some sensitivity on the error floors assigned for the measured velocities of the masers. Currently, we adopt an error floor of 0.4 km s^{-1} for the velocities of high-velocity masers and 0.8 km s^{-1} for those of systemic masers. These numbers are estimates based on our understanding and experience of the effects of astrophysical noise and degree of maser line blending, and could be uncertain for about a few $\times 0.1 \text{ km s}^{-1}$. By exploring the variations in the best-fit H_0 with different error floors for the maser velocities, the fitted H_0 could change as much as $5 \text{ km s}^{-1} \text{ Mpc}^{-1}$. We consider this as systematic error. After including this value in the total uncertainty budget, our data gives a Hubble constant of $H_0 = 74 \pm 10 \text{ km s}^{-1} \text{ Mpc}^{-1}$. We show the rest of the fitting results in Table 5.

4.3. The Angular-diameter Distance to NGC 6264

In the modeling of the maser disk, we use H_0 instead of D as one of the fitting parameters, as explained in the appendix. In order to obtain the posteriori probability distribution for the maser distance to NGC 6264, we calculate D with the equation $D = v_{sys}/H_0$ for each Markov-chain trial in the Bayesian modeling, and compute the posteriori probability distribution for D afterward. The right panel of Figure 7 shows the posteriori probability distribution for D . The distribution appears to be asymmetric with a long tail toward the large distance end. This tail is a natural result of H_0 being in the denominator of $D = v_{sys}/H_0$, with H_0 having a substantial and roughly equal 68% uncertainty on either side of the peak of the posteriori probability distribution. The posteriori probability distribution of D has a 68% confidence range of 16 Mpc centered at $D = 137$ Mpc. Since H_0 has a systematic error of $\sim 5 \text{ km s}^{-1} \text{ Mpc}^{-1}$ caused by the error floor uncertainties for maser velocities, we add the corresponding systematic uncertainty in the distance (9 Mpc) in quadrature to the error derived from the posteriori probability distribution, and the total uncertainty becomes 19 Mpc.

5. Discussion

5.1. The First Geometric Distance to A Galaxy Beyond 100 Mpc

Traditionally, Hubble constant determinations relied on indirect distance measurements through the Extragalactic Distance Ladder (EDL), which bases its calibration on the Period-Luminosity (PL) relation of Cepheid variables. In the past, the need to appeal to the EDL was inevitable because direct distance determinations were limited to stars in the Milky Way, the Large Magellanic Cloud, and water masers in NGC 4258 (Distance = 7.2 ± 0.5 Mpc; Herrnstein et al. 1999). Direct distance measurements to galaxies in the Hubble flow (Distance > 50 Mpc) have never been achieved until recently (e.g. Braatz et al. 2010; Suyu et al. 2010; Reid et al. 2012).

In this paper, we obtain the first direct measurement of *angular-diameter* distance to a galaxy beyond 100 Mpc in a single step without any local calibration. NGC 6264 is more than 15 times farther than NGC 4258, and the angular size of the maser disk is more than 10 times smaller. In addition, the maser flux densities are over 100 times fainter. The small size (~ 1.4 mas in diameter) and the low flux densities of these maser disks have not only been a big issue for efficient VLBI imaging and accurate astrometry, but also make reliable acceleration measurements difficult because of low signal-to-noise ratio. Moreover, instead of residing in a single narrow ring as in NGC 4258, the systemic masers in NGC 6264 are located in multiple radii. This prevents using the simple approach adopted for measuring the distance to UGC 3789 (Braatz et al. 2010), and instead we use the more sophisticated 3-dimensional modeling for this megamaser disk. The work presented in the previous MCP papers (Braatz et al. 2010; Kuo et al. 2011), Reid et al. (2012), and this paper shows the effort to face these challenges by developing the 3-dimensional Bayesian modeling program and the new ways to perform VLBI self-calibration and global acceleration fitting. It is because of these efforts that make sensitive VLBI imaging and accurate distance/Hubble constant determination possible.

6. Summary

Our main conclusions are the following:

1. We modeled the H₂O maser disk in NGC 6264 with Bayesian analysis, and obtain a Hubble of $H_0 = 73.3 \pm 10.3 \text{ km s}^{-1} \text{ Mpc}^{-1}$ and an angular-diameter distance of $136.5 \pm 16.3 \text{ Mpc}$. The Hubble constant is consistent with the value obtained in Paper II ($H_0 = 69 \pm 11$) as well as the Cepheid-based H_0 from Freedman & Madore (2010; $H_0 = 73 \pm 4$) and Riess et al. (2011; $H_0 = 74 \pm 2$). This is the first time the megamaser technique has been successfully applied to a galaxy beyond 100 Mpc.
2. The application of the megamaser technique to galaxies deep in the Hubble flow is intrinsically more difficult because of significantly lower flux densities and smaller disk angular size, and these factors make precise astrometry and acceleration measurements more challenging. In order to image the maser disks in distant galaxies more efficiently, utilizing multiple maser lines at different locations of the maser disk with the self-calibration technique developed in this work to enhance the signal-to-noise ratio may often be necessary.
3. The measured accelerations suggest that the maser disk in NGC 6264 appears to have more substructure than the masers in UGC 3789 and NGC 4258. The systemic masers are located at least at five different radii from the BH. Full 3-Dimensional modeling is essential to measure the distance to NGC 6264 because of the complexity of the maser disks.

In the future, we expect that with the new observations included in the analysis, we would be able to improve the accuracy of the distance measurement to better than 10%, and explore the impact of orbital eccentricity on the distance measurement

A. Correlation Between Distance or H_0 and Black Hole Mass Estimates

In our Bayesian modeling of maser disks in the MCP, we fit H_0 directly, rather than fitting D as in Herrnstein et al. (1999). There are four reasons that make H_0 preferable over D in the disk modeling: (1) since H_0 is the primary parameter we intend to measure, it is more convenient to save an extra step of calculation and have the posteriori probability distribution of H_0 directly output from the modeling program; (2) in this way the effect of uncertainty in peculiar velocity of a galaxy can be directly incorporated in the H_0 calculation; (3) since $D \propto 1/a_{sys}$ and a_{sys} usually has the largest fractional uncertainty among our observables, as a result, the posteriori probability distribution function of D would usually be asymmetric even when the data quality is high; finally, (4) if we use D as a fitting parameter, its posteriori probability distribution is usually highly correlated with M_{BH} (See Figure 8a), typically about 0.99 or even 1.

Such a high correlation coefficient between D and M_{BH} implies that these parameters may be degenerate, and the fitting result in such a circumstance might not be reliable. This problem was not recognized in previous work on NGC 4258 by Herrnstein et al. (1999). We found that replacing D with H_0 in Bayesian modeling resolves this issue; the absolute value of the correlation coefficient between H_0 and M_{BH} is significantly less than one. Nonetheless, the nearly perfect correlation between D and M_{BH} deserves some further investigation in order to understand its nature and whether the results from the work on NGC 4258 and from our initial modelings that fit the maser disks with D and M_{BH} are reliable. In the following analysis, we use a "simple" maser disk with systemic masers lying in a single narrow ring to demonstrate that the nearly perfect correlation between D and M_{BH} is not a sign of degeneracy, and is just a result of substantial discrepancies between uncertainties of different observables.

In the problem of modeling the maser disk and determining the angular-diameter distance, the relationship between D and M_{BH} arises from two different measurements : the centripetal acceleration of the

systemic masers and the Keplerian rotation curve for the high velocity masers. In the former case, we can see the relation between D and M_{BH} in the equation for the centripetal acceleration a_{sys} :

$$a_{sys} = \frac{GM_{BH}}{r^2} = \frac{GM_{BH}}{D^2 \Delta\theta^2}, \quad (A1)$$

where G is the gravitational constant, r is the physical radius of the orbit of the systemic masers, and $\Delta\theta$ is the apparent angular radius of the systemic masers. In principle, $\Delta\theta$ can be obtained from the intersection points between the straight line traced by systemic masers ($V = \Omega \theta$) and the Keplerian rotation curve traced by the high velocity masers ($V = k \theta^{-1/2}$) in the position-velocity diagram of the maser disk (see Braatz et al. 2010). By solving for $\Delta\theta$ with the rotation curves for the systemic and high-velocity masers, we obtain $\Delta\theta = (k/\Omega)^{2/3}$. With this, we can re-write Equation (A1) and express M_{BH} as a quadratic function of D :

$$M_{BH} = \frac{a_{sys}}{G} \left(\frac{k}{\Omega} \right)^{4/3} D^2. \quad (A2)$$

On the other hand, since the coefficient k of the Keplerian rotation curve is defined as $k \equiv \sqrt{GM_{BH}/D}$, we can also find a linear relationship between D and M_{BH} as

$$M_{BH} = \left(\frac{k^2}{G} \right) D. \quad (A3)$$

In Figure 8b, we plot Equation (A2) with black quadratic curves and Equation (A3) with blue straight lines for a given set of measurements of a_{sys} , k , and Ω including their uncertainties. Every intersection of a blue line and a black curve (red dots in Figure 8b) represents a solution for D and M_{BH} from fitting the maser disk, and all possible solutions (within one σ uncertainty) only fall in a region on the $D - M_{BH}$ diagram whose shape is defined by the relative sizes of the uncertainties in a_{sys} , k , and Ω . In current megamaser galaxies being observed for distance determination, the uncertainty in k is usually negligible ($\sim 1\%$) while the errors in a_{sys} and Ω are more significant (e.g. $\geq 10\%$). As a result, the blue lines span a very narrow region on the $D - M_{BH}$ diagram while the black curves cover a much broader region, and all the possible solutions for D and M_{BH} fall on a region whose shape resembles a line. This makes D and M_{BH} appear to be nearly 100% correlated. Therefore, the apparent high correlation between D and M_{BH} from the modeling program is not a result of intrinsic degeneracy, and thus the fitting results should be reliable.

In Figure 8c, we demonstrate how the high correlation between fitting parameters is removed by replacing D with V_{sys}/H_0 in Equations (A2) & (A3). Now, one can see that the possible solutions no longer fall exactly on a straight line, and actually follow the $M_{BH} \propto 1/H_0$ relationship. Because of this, the nearly perfect correlation doesn't exist between M_{BH} and H_0 . Nonetheless, one can imagine that if the uncertainties in a_{sys} and Ω are also small, then the black curves may cover a much smaller region, and the possible solutions may only fall in a small segment of the $1/H_0$ curve. The distribution would thus resemble a straight line, and high parameter correlation appears again. This is indeed seen in our data, but because of the analysis shown here, high correlation should no longer be a serious concern.

The National Radio Astronomy Observatory is a facility of the National Science Foundation operated under cooperative agreement by Associated Universities, Inc. We thank Ed Fomalont for his kind help with our VLBI data reduction and Lincoln Greenhill for his substantial assistance for this project. C.Y. Kuo thanks Mark Whittle for his numerous insightful comments on our project. This research has made use of NASA's Astrophysics Data System Bibliographic Services, and the NASA/IPAC Extragalactic Database

(NED) which is operated by the Jet Propulsion Laboratory, California Institute of Technology, under contract with the National Aeronautics and Space Administration.

Should thank Treu for his comments on radiation pressure as a source of systematic error.

REFERENCES

- Argon, A. L., Greenhill, L. J., Reid, M. J., Moran, J. M., Humphreys, E. M. L. 2007, *ApJ*, 659, 1040
- Beers, T. C.; Kriessler, J. R.; Bird, C. M.; Huchra, J. P. 1995, *AJ*, 109, 874
- Braatz, J., Condon, J., Reid, M., Henkel, C., Lo, K. Y., Kuo, C. Y., Impellizzeri, C., Hao, L. The Megamaser Cosmology Project Large Proposal, submitted to NRAO June 1, 2009
- Braatz, J. A., Reid, M. J., Humphreys, E. M. L., Henkel, C., Condon, J. J., & Lo, K. Y. 2010, *ApJ*, in press
- Freedman, W. L. et al. 2001, *ApJ*, 553, 47
- Freedman, W. L.; Madore, Barry F. 2010, *ARA&A*, 48, 673
- Frieman, J. A., Turner, M. S., Huterer, D. 2008, *ARA&A*, 46, 385
- Greenhill, L. 2009, *Astro2010: The Astronomy and Astrophysics Decadal Survey*, Science White Papers, 103
- Herrnstein, J. R., Moran, J. M., Greenhill, L. J., Diamond, P. J., Inoue, M., Nakai, N., Miyoshi, M., Henkel, C., Riess, A. 1999, *Nature*, 400, 539
- Hu, W. 2005, *ASPC*, 339, 215
- Humphreys, E. M. L., Reid, M. J., Greenhill, L. J., Moran, J. M., Argon A. L. 2008, *ApJ*, 672, 800
- Kuo, C. Y., Braatz, J. A., Condon, J. J., Impellizzeri, C. M. V., Lo, K. Y., Zaw, I., Schenker, M., Henkel, C., Reid, M. J., Greene, J. E. 2011, *ApJ*, 727, 20
- Kuo, C.-Y. 2012, Ph.D. thesis, University of Virginia
- Perlmutter et al. 1999, *ApJ*, 517, 565
- Reid, M. J., Braatz, J. A., Condon, J. J., Greenhill, L. J., Henkel, C., Lo, K. Y. 2009, *ApJ*, 695, 287
- Reid, M. J., Braatz, J. A., Condon, J. J., Kuo, C. Y., Impellizzeri, C. M. V., & Henkel, C. 2012 in prep.
- Riess et al. 1998, *AJ*, 116, 1009
- Riess, A. G., Macri, L., Casertano, S., Lampeitl, H., Ferguson, H. C., Filippenko, A. V., Jha, S. W., Li, W., Chornock, R. 2011, *ApJ*, 730, 119
- Suyu, S. H., Marshall, P. J., Auger, M. W., Hilbert, S., Blandford, R. D., Koopmans, L. V. E., Fassnacht, C. D., Treu, T. 2010, *ApJ*, 711, 201

3D Bayesian Fitting

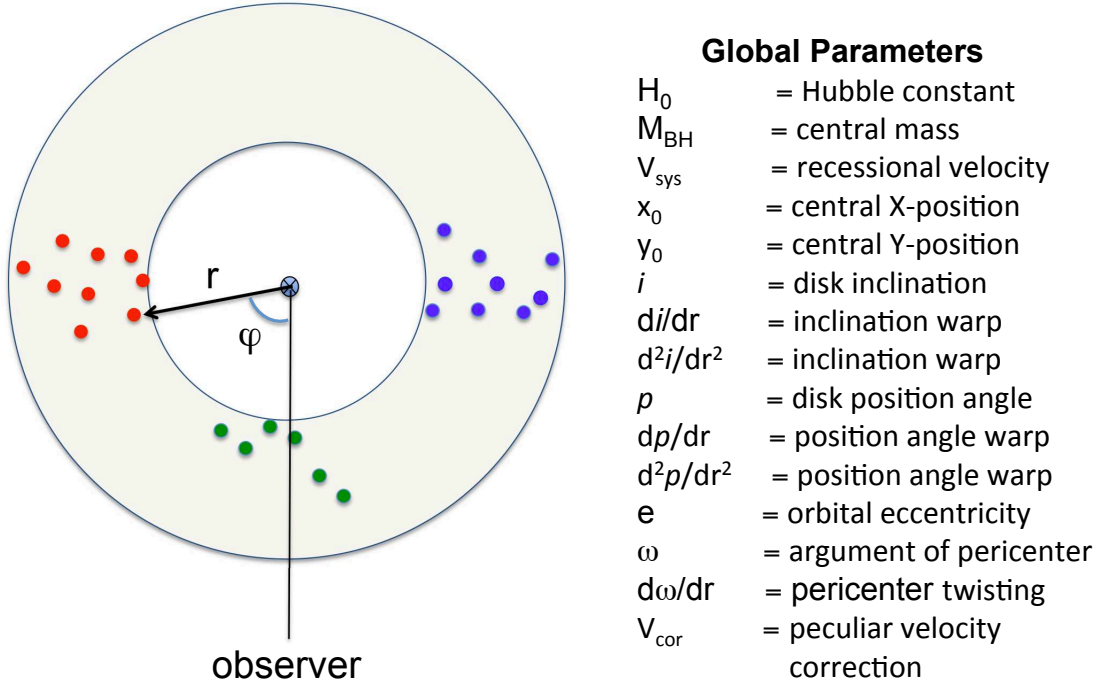


Fig. 4.— The model and parameters for Bayesian fitting of maser disks in the MCP. The cartoon plot on the left shows the model maser disk around a supermassive BH at the center. The model maser spots are allowed to be at any locations on the disk plane. The fitting program can fit elliptical orbits, but in this paper we model the masers in circular orbits. In the plot, r and ϕ denote the radius and disk azimuth angle of a maser spot with $\phi \approx 0^\circ$ for systemic masers (green spots) and $\phi \approx -90^\circ$ or 90° for redshifted (red spots) or blueshifted (blue spots) masers. The 15 parameters on the right are the parameters that one can use to fit a maser disk. Among these parameters, H_0 , M_{BH} , v_{sys} , x_0 , y_0 , i , and p are the most important and necessary for Hubble constant determination. Whether other parameters should be included in the modeling would depend on degree of disk warping, circularity of maser orbits, and whether one wants to include uncertainty of galaxy peculiar velocity in the calculation.

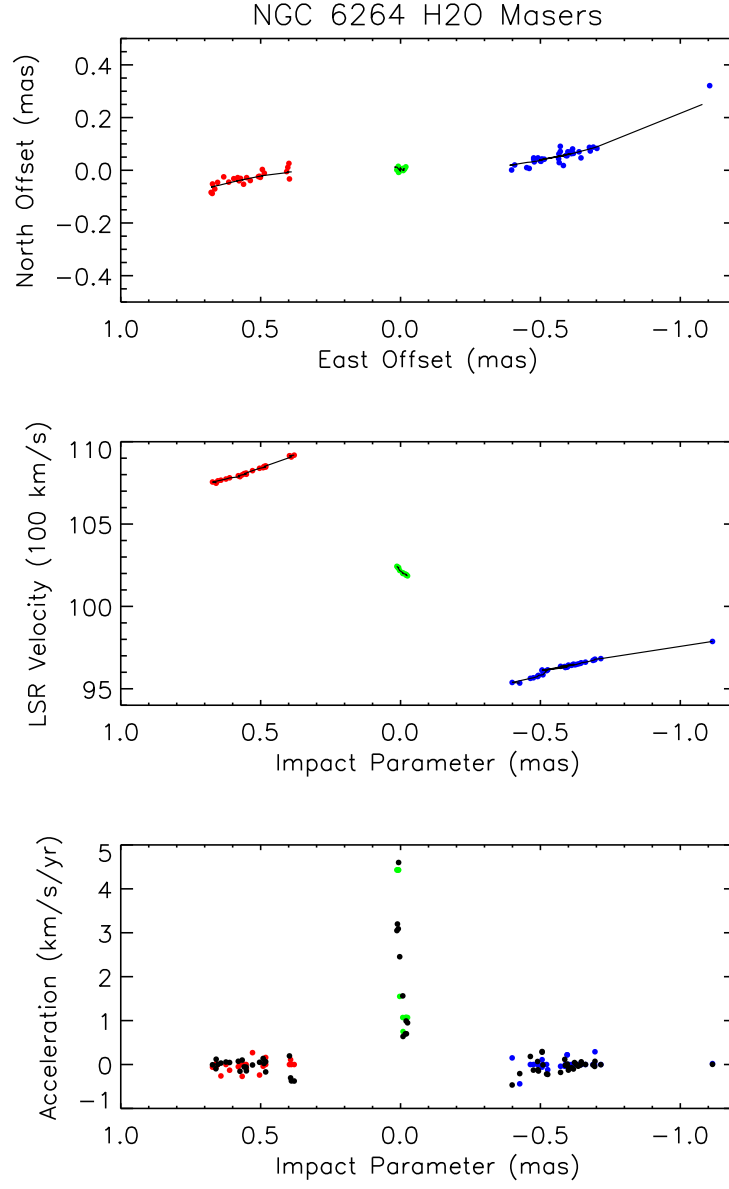


Fig. 5.— Data (colored dots) and best-fit model (lines and black dots). Top panel: Positions on the sky. Middle panel: LSR velocity versus position along the disk. Bottom panel: Accelerations versus impact parameter.

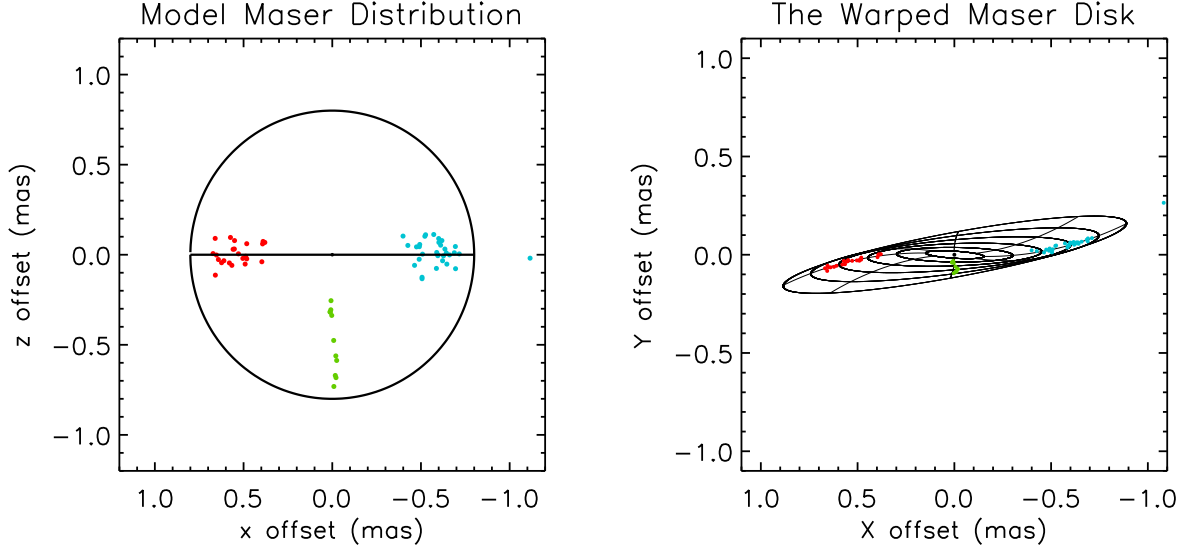


Fig. 6.— The left panel shows the model maser distribution in NGC 6264 from the overhead perspective. The right panel shows the best-fit warp from the observer’s perspective with model maser spots plotted on top of it. For illustration, we decrease the disk inclination by $\sim 5^\circ$ to show the degree of disk warping more clearly.

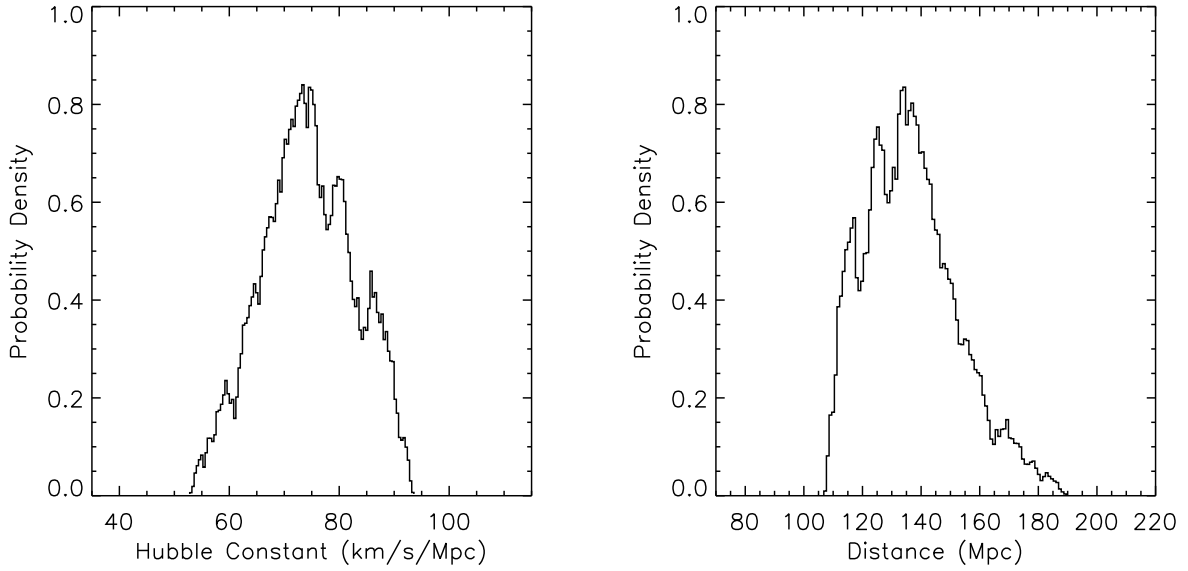


Fig. 7.— The left and right panel show the posteriori probability distribution of the Hubble constant H_0 and the distance to NGC 6264, D , respectively. The posteriori probability distribution of H_0 has a 68% confidence range that centers at $H_0 = 74.3 \text{ km s}^{-1} \text{ Mpc}^{-1}$ with an uncertainty of $9.0 \text{ km s}^{-1} \text{ Mpc}^{-1}$ while that of D has a 68% confidence range that centers at $D = 137 \text{ Mpc}$ with an uncertainty of 16 Mpc .

Table 6. NGC 6264 H₂O Maser Model

Parameter	Priors	Posterioris	Units
H_0	72±18	74±10	km s ⁻¹ Mpc ⁻¹
V_{sys}	10196±28	10209±2	km s ⁻¹
V_{cor}	-19±300	-24±291	km s ⁻¹
M_{BH}	3.45	2.89±0.39	10 ⁷ M_\odot
x_0	0.006	0.008±0.003	mas
y_0	0.006	0.007±0.003	mas
i_0	88.5	88.8±2	deg
i_1	1.9	1.0±2.7	deg mas ⁻¹
p_0	83.3	84.0±1.5	deg
p_1	18.8	17.8±2.1	deg mas ⁻¹

Note. — Parameters are as follows: Hubble constant (H_0), V_{LSR} of central black hole (V_{sys}), peculiar velocity with respect to Hubble flow in cosmic microwave background frame (V_{cor}), black hole mass (M_{BH}), eastward (x_0) and northward (y_0) position of black hole with respect to the average position of the systemic maser features from the BB261K and BB261Q data, disk inclination (i_0) and inclination warping (change of inclination with radius: $i_1 \equiv di/dr$), disk position angle (p_0) and position angle warping (change of position position angle with radius: $p_1 \equiv dp/dr$). Flat priors are listed without uncertainties; otherwise Gaussian sigmas are listed.

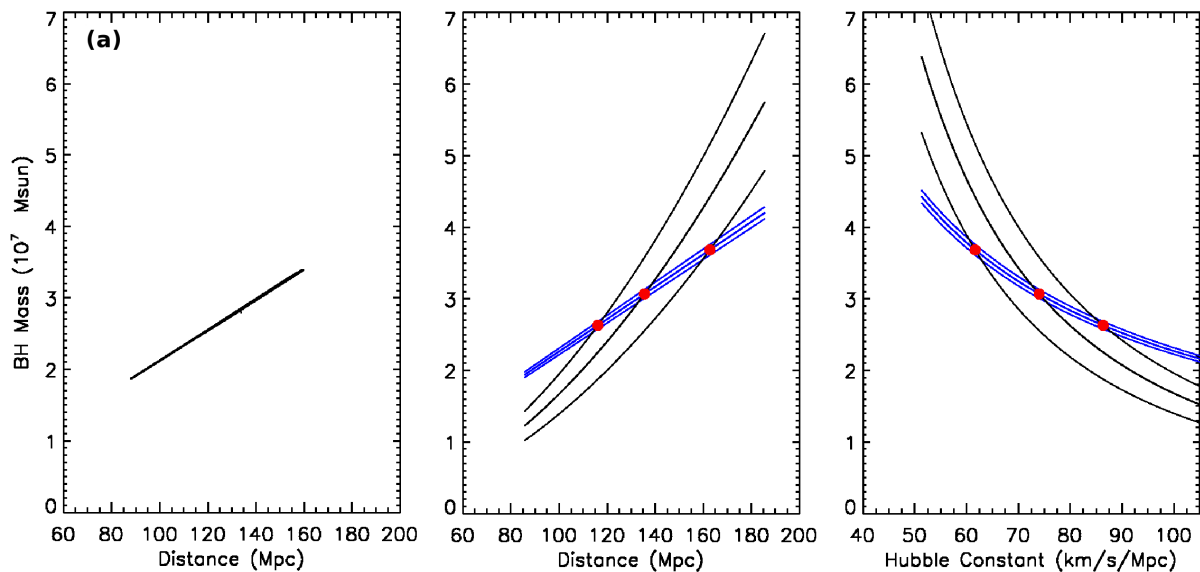


Fig. 8.— We illustrate the apparent correlation between D and M_{BH} and the possible cause. The left panel shows the fitting results for galaxy distance D and BH mass M_{BH} from our initial version of the Bayesian fitting program plotted on the $D - M_{BH}$ diagram. The nearly straight-line appearance shows that D and M_{BH} are highly correlated, and the correlation coefficient is usually about 0.99 or even 1.0. The plot shown in the middle panel provides an explanation for this correlation. The black curves represent the quadratic relation between D and M_{BH} from Equation (A2) and the blue straight lines show the linear relation for D and M_{BH} from Equation (A3) for a given set of measurements of a_{sys} , k , and Ω . For a given distance, the black curves (from top to bottom) give the M_{BH} measured with a_{sys} , k , and Ω , plus its 1σ , 0σ and -1σ uncertainty. Likewise, the blue lines (from top to bottom) give the measured M_{BH} based on Equation (A3) plus its 1σ , 0σ , and -1σ uncertainty. Every intersection of a blue line and a black curve (the red spots) represents a solution for D and M_{BH} from fitting the maser disk. From the discussion in the appendix, we conclude that it is because the uncertainty in k is usually significantly smaller than a_{sys} and Ω that all solutions fall nearly on a straight line on the $D - M_{BH}$ diagram. The presentation in the right panel is similar to that of the middle panel, with the only difference that D in Equation (A2) and (A3) is replaced by v_{sys}/H_0 , and we plot the Hubble constant in the x-axis. It can be seen that the solutions no longer fall on a straight line, and H_0 and M_{BH} are not perfectly correlated.